

Non-linear Model-based Control of Neural Cell Dynamics

Rongting Yue (✉ rongting.yue@uconn.edu)

University of Connecticut

Ryan Tomastik

University of Connecticut

Abhishek Dutta

University of Connecticut

Research Article

Keywords: Neurons, Non-linear, neural cell, model-based control, dynamics

Posted Date: May 27th, 2022

DOI: <https://doi.org/10.21203/rs.3.rs-580874/v2>

License: © ⓘ This work is licensed under a Creative Commons Attribution 4.0 International License.

[Read Full License](#)

Non-linear Model-Based Control of Neural Cell Dynamics

Rongting Yue^{1,*}, Ryan Tomastik¹, and Abhishek Dutta¹

¹University of Connecticut, Electrical and Computer Engineering, Storrs, 06269, United States

*rongting.yue@uconn.edu

ABSTRACT

The human brain consists of 100 billion neurons connected to each other with synapses, with more than 10 thousand of them per neuron. When a neuron reaches a threshold voltage, due to the summation of currents flowing in from synapses or by external stimulation, the neuron fires with an action potential, observed as a voltage spike. It is this nonlinear firing behavior together with firing rate that gives rise to synaptic plasticity and forms the basis of memory, perception, action, and behavior. A perturbed firing of the underlying neuron can therefore evolve into undesirable mental states linked to various neurological disorders. Closed-loop control of the firing rate of the neuron is thus desirable, but very challenging due to the underlying highly nonlinear dynamics. A Hodgkin-Huxley model of the nonlinear neural dynamics in terms of its membrane potential with respect to current stimulation is developed together with its underlying ion channel dynamics in terms of gating variables. The model is linearized at operating point and lead, lag and lead-lag compensators are synthesized. Next, a dynamic inversion nonlinear controller, a robust incremental dynamic inversion controller, and a model predictive controller are derived to directly regulate the nonlinear neuron dynamics in terms of controlled firing. The synthesis of lead, lag, lead-lag, dynamic inversion, model predictive control-based feedback controllers over the nonlinear dynamics of the neuron led to controlled firing and a fast response that was robust to stochastic synaptic noise.

Introduction

Neurons, the nerve cells in our brains¹, can have more than millions of connections to other neurons. These neurons are made up of the cell membrane, axons, dendrites, and synapses. A synapse is a small gap across which one neuron will send information to another neuron in the form of electric current. The end of the neuron that is sending the signal is the axon, and the receiving end of the neuron is the dendrite. The act of sending a current across a synapse is referred to as neuron firing, and it occurs when the electric potential of the membrane, V_m , reaches a certain threshold voltage, causing a spike in the voltage. This activity is caused by the moving of ions into and out of the neuron through the cell membrane, specifically sodium and potassium ions. At the threshold voltage, sodium gates open allowing sodium ions to flood in until a peak voltage is reached. It is at this time that the potassium gates open allowing potassium ions to flow out of the neuron, causing the potential to return to its resting state. Figure 1 shows a simple model of a neuron.

Controlling the firing rate of a neuron has numerous applications to various neurological diseases. It has already been shown that control systems can be used to help people with seizures²⁻⁷ and to artificially recreate the experience of touch⁸. Another application is the control of neural oscillation and the blocking of neuron firing, which has been shown to be helpful in the treatment for diseases such as Parkinson disease or epilepsy⁹⁻¹¹. Controlling a neuron to affect the motor functions of animals such as molluscs and insects is another application^{12,13}. Additionally it has been shown that controlled electrical stimulation as a treatment for migraines¹⁴. In general, electrical stimulation to control action potential can potentially restore functions that an individual has lost, such as vision or hearing¹⁵⁻¹⁷.

Various researchers have considered the problem of controlling the dynamics of neurons in great detail. One method is to base the model around the Hodgkin-Huxley (HH) equations, which are four coupled and nonlinear differential equations that describe a change in the membrane voltage of a neuron¹⁸⁻²³. Other researches have instead designed their models around the integrate-and-fire method²⁴⁻²⁶.

As for the controllers themselves, there has been work into using open loop and closed loop strategies to control how a neuron fires (for example, ²⁷⁻³⁸). Some researchers have used model predictive control, a form of linear feedback control, to design their controller¹⁸, while others have used feedforward control^{9,39}. Also used has been a series of adaptive controllers which allows one to tune the controller at different stages of design³⁹. However, what is lacking is the design and application of combination of lead and lag controllers and robust incremental dynamic inversion based control synthesis to achieve controlled spiking of the nonlinear dynamics of neuron in spite of synaptic noise. Also, the linear model predictive control used in¹⁸ was performed on specific operating points, whose performance of tracking accuracy may be degraded by the gaps between the

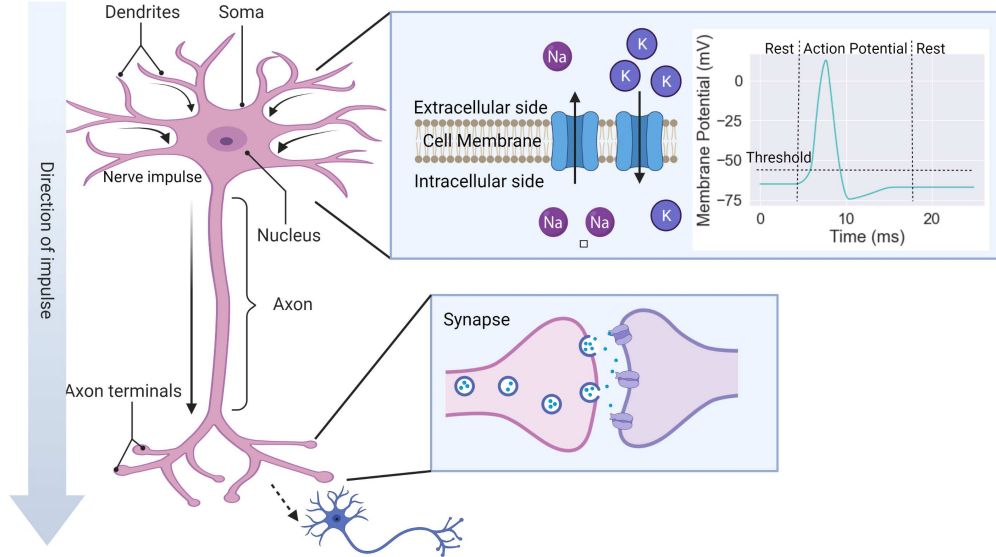


Figure 1. A schematic of the neuron. Once the cell membrane reaches the threshold voltage, ions channels open allowing sodium and potassium ions to flow in and out, respectively. This results in the membrane voltage to spike, and an electric current moves across the synapse and is received by another neuron; this is how information is sent from neuron to neuron. The axon is the part of the neuron that carries the current away from the neuron, while the dendrite is what receives the current.

linearized models on different operating points.

In this paper, we consider the nonlinear HH model of the neuron together with equations for its underlying ion channels and gate dynamics. Next, lead, lag and lead-lag compensators are synthesized over linearized dynamics of the neuron based on desired specifications. This is followed by the derivation of a dynamic inversion nonlinear controller, a robust incremental dynamic inversion controller, and a model predictive controller. These model based controllers are then used to regulate the firing of the nonlinear neural dynamics in the presence of stochastic synaptic noise. The results are encouraging in terms of the ability to generate a controlled spike and are compared in the light of precision and speed of response.

Methods

The Hodgkin-Huxley Model

The HH equations are four coupled non-linear differential equations which describe the change in V_m . The equations take this V_m to be dependent on the input current, I_{inj} . Figure 2 shows the circuit representation of the neuron as described. The current of the flow of potassium ions is described by a conductance of G_K , a voltage of E_K which describes the potassium ion separation, and the term n which describes the behavior of the potassium gates opening. Similarly, we can define terms for sodium: G_{Na} , E_{Na} , m , and h . Notice that to describe the opening of sodium gates, two terms m and h are required. The terms G_m and V_{leak} describe the current of the remaining ions. The conductances depend on the voltage, while the current sources do not. A capacitor is included in parallel to represent the cell membrane, which behaves as a capacitor. Summing the currents in each component of the circuit gives Equation (1):

$$C_m \frac{dV_m}{dt} = G_K n^4 (E_K - V_m) + G_{Na} m^3 h (E_{Na} - V_m) + G_m (V_{leak} - V_m) + I_{inj} \quad (1)$$

with constants defined as $G_{Na} = 120 \frac{mS}{cm^2}$, $G_K = 36 \frac{mS}{cm^2}$, $G_m = 0.3 \frac{mS}{cm^2}$, $E_{Na} = -115mV$, $E_K = 12mV$, $V_{leak} = -10.613mV$, and $C_m = 1 \frac{mF}{cm^2}$.

This equation is clearly non-linear, since m , n , and h are all variables representing the potassium gate activation, sodium gate activation, and sodium gate inactivation, respectively. They take on continuous values between zero and one representing the fraction of the channels in the corresponding state. They are described by first-order differential equations that depend on parameters α_n , β_n , α_m , β_m , α_h , and β_h who each in turn depend non-linearly on the displacement of the membrane potential

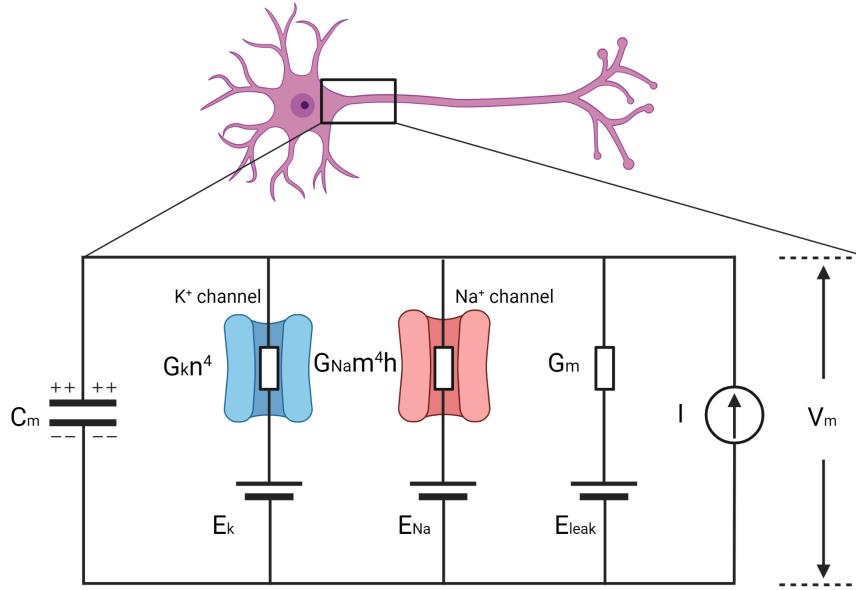


Figure 2. The circuit representation of the current flowing through a neuron membrane as described by the HH equations. The total current in the neuron is the sum of the current of each component of the circuit: the capacitor, the potassium, the sodium, a leakage current (G_m), and the injected current, I . The conductances G_K , G_{Na} , and G_m represent the ion channels and the voltage sources E_K , E_{Na} , and E_{leak} represent the equilibrium potentials.

voltage, V . The equations are given as:

$$\begin{aligned} \frac{dn}{dt} &= \alpha_n(V_m)(1-n) - \beta_n(V_m)n, \\ \frac{dm}{dt} &= \alpha_m(V_m)(1-m) - \beta_m(V_m)m, \\ \frac{dh}{dt} &= \alpha_h(V_m)(1-h) - \beta_h(V_m)h, \end{aligned} \quad (2)$$

$$\begin{aligned} \alpha_n(V_m) &= \frac{10 - V_m}{100(e^{\frac{10-V_m}{10}} - 1)}, \\ \beta_n(V_m) &= 0.125e^{-\frac{V_m}{80}}, \\ \alpha_m(V_m) &= \frac{25 - V_m}{10(e^{\frac{25-V_m}{10}} - 1)}, \\ \beta_m(V_m) &= 4e^{-\frac{V_m}{18}}, \\ \alpha_h(V_m) &= 0.07e^{-\frac{V_m}{20}}, \\ \beta_h(V_m) &= \frac{1}{e^{\frac{30-V_m}{10}} + 1} \end{aligned} \quad (3)$$

Equations (1), (2), and (3) are given in the reference⁴⁰.

Linearization

To begin analysis of this system, it will be linearized. We shall define the state space $x \in \mathbb{R}^4$ to be

$$\vec{x}^T = [V_m \quad n \quad m \quad h] \quad (4)$$

The system is nonlinear, thus it may behave differently around different points and linearizing around one operating point may not be enough to describe the behavior of the entire system. The system will therefore be linearized at multiple operating points

(V_o, n_o, m_o, h_o) . In general, the linearized state space of the system can be represented in the form

$$\dot{\vec{x}} = A\vec{x} + Bu, \vec{y} = C\vec{x} \quad (5)$$

where the input, u , is the injected current I_{inj} , and

$$A = \begin{bmatrix} A_{11} & A_{12} & A_{13} & A_{14} \\ A_{21} & A_{22} & 0 & 0 \\ A_{31} & 0 & A_{33} & 0 \\ A_{41} & 0 & 0 & A_{44} \end{bmatrix} \quad (6)$$

$$B = \begin{bmatrix} 1 \\ 0 \\ 0 \\ 0 \end{bmatrix} \quad (7)$$

and

$$C = [1 \ 0 \ 0 \ 0] \quad (8)$$

where

$$\begin{aligned} A_{11} &= \frac{-G_K n_o^4 - G_{Na} m_o^3 h_o - G_m}{C_m}, \\ A_{12} &= \frac{4G_K n_o^3 (E_K - V_o)}{C_m}, \\ A_{13} &= \frac{3G_{Na} m_o^2 h_o (E_{Na} - V_o)}{C_m}, \\ A_{14} &= \frac{G_{Na} m_o^3 (E_{Na} - V_o)}{C_m}, \\ A_{21} &= \frac{-10(e^{\frac{10-V_o}{10}} + 1)}{(100(e^{\frac{10-V_o}{10}} - 1))^2} (1 - n_o) - 0.0015625e^{-V_o} 80n_o, \\ A_{22} &= -\frac{10 - V_o}{100(e^{\frac{10-V_o}{10}} - 1)} - 0.125e^{\frac{-V_m}{80}}, \\ A_{31} &= \frac{-e^{\frac{25-V_o}{10}} V_o + 15e^{\frac{25-V_o}{10}} + 1}{(10(e^{\frac{25-V_o}{10}} - 1))^2} (1 - m_o) - \frac{2}{9}e^{\frac{-V}{18}} m_o, \\ A_{33} &= -\frac{25 - V_m}{10(e^{\frac{25-V_m}{10}} - 1)} - 4e^{\frac{-V_m}{18}}, \\ A_{41} &= -0.0035e^{\frac{-V_o}{20}} (1 - h_o) + \frac{e^{\frac{30-V_o}{10}}}{10(e^{\frac{30-V_o}{10}} + 1)^2} h_o, \\ A_{44} &= -0.07e^{\frac{-V_m}{20}} - \frac{1}{e^{\frac{30-V}{10}} + 1} \end{aligned} \quad (9)$$

With this general form, the system can be linearized on multiple operating points, (V_o, n_o, m_o, h_o) , in between the resting potential (-70 mV) and the threshold potential (about -55 mV). The relative baseline voltage of V_o varies. In this work, we pick the absolute membrane voltage of around -70 mV as the baseline (i.e., $V_o = 0$ mV).

Four test values are arbitrarily chosen to observe the difference in behavior. These points have absolute membrane voltages of -70 , -65 , -60 , -56 , all in millivolts, corresponding to relative voltages of 0 mV, 5 mV, 10 mV, 14 mV, with each voltage producing a different value for n_o , m_o , and h_o given by Equation (11). The response of each linearized system to a current step of $I_{inj} = 8$ nA is shown in Figure 3. Clearly the behavior does not change significantly enough to justify using multiple operating points. Furthermore, as will be shown later in this paper, designing a controller for the system linearized around one operating point meets the desired control objectives on the nonlinear system. Thus controllers will be designed for the system

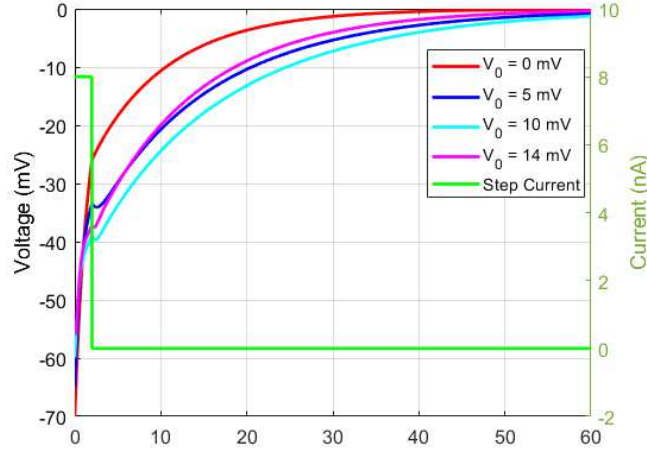


Figure 3. Step responses of the linearized system. (For visualization purpose, the time response of voltages are transformed from relative displacement to absolute membrane voltages. And this transformation will be used in all the following plots of the time response simulation.) Four different operating points were chosen (between the resting voltage -70 mV and the threshold voltage -55 mV) to determine how the behavior of the system changed. From this four transfer functions were calculated, and their response to a step current ($I_{inj} = 8$ nA) is plotted here.

linearized about the point $(0, 0.3177, 0.0529, 0.5961)$, with transfer function of output membrane voltage (mV) to input current (nA) $G(s)$ shown in Equation (10).

$$G(s) = \frac{s^3 + 4.524s^2 + 1.291s + 0.0909}{s^4 + 5.201s^3 + 4.301s^2 + 0.7726s + 0.03894} \quad (10)$$

$$\begin{aligned} n_o &= \frac{\alpha_n(V_o)}{\alpha_n(V_o) + \beta_n(V_o)}, \\ m_o &= \frac{\alpha_m(V_o)}{\alpha_m(V_o) + \beta_m(V_o)}, \\ h_o &= \frac{\alpha_h(V_o)}{\alpha_h(V_o) + \beta_h(V_o)} \end{aligned} \quad (11)$$

Clearly this linearized system is stable, as the poles are all in the left hand plane. The plot for $V_o = 0$ mV in Figure 3 also shows this. Now, controllers can be designed for this system.

Lead and Lag Compensator

Lead Compensator

The objective is to control the membrane voltage by injecting current into the neuron, with the ultimate goal being to cause an activation spike by having the membrane voltage reach the threshold voltage of about -55 mV. From the transfer function in Equation (10) it can immediately be seen that the system is stable, as the poles are all in the left hand plane. A lead compensator is designed with general form $G_d(s) = k_c \frac{s+z}{s+p}$, where z is the zero, p is the pole, and k_c is the gain. To begin, the Bode plot of $G(s)$ is examined, shown in Figure 4. The phase margin here is already high, so the design will keep it as such. The desired phase margin is $PM \geq 131$ degrees, with a bandwidth frequency of $\omega_{bw} = \omega_c \geq 10$ radians/second. This will increase the speed of the transient response because the crossover frequency is being increased. Unlike a lag compensator, a lead compensator does not take the steady state error into account during the design of the controller.

To begin the design of the compensator, Figure 4 is examined and the phase of the transfer function at the desired crossover frequency, denoted as $\angle G(j\omega_c)$, must be found. This is found to be -86.2 degrees. Then the required phase lead, ϕ_m , can be found and the lead compensator pole and zero can be calculated as follows:

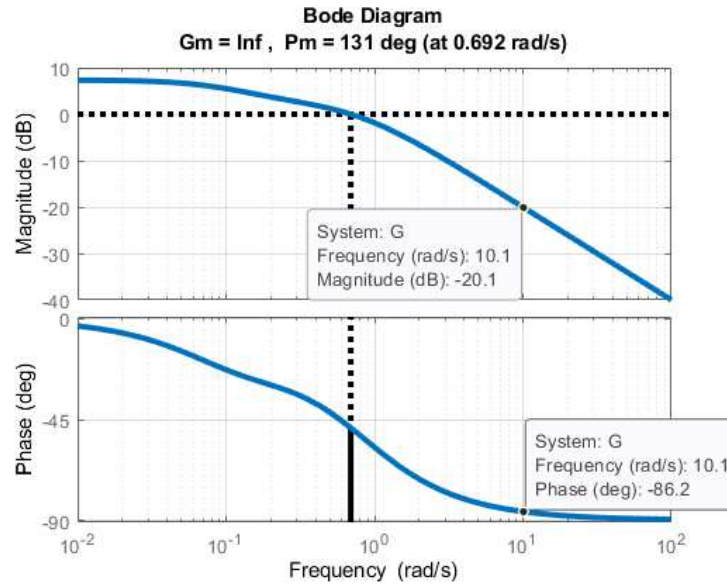


Figure 4. The Bode plot of the transfer function of the linearized system, G , is shown here. The Bode plot was used in designing lead, lag, and lead-lag controllers.

$$\phi_m = PM - (180 + \angle H_0(jw_c)) = 37.2^\circ \quad (12)$$

$$\frac{z}{p} = \frac{1 - \sin(\phi_m)}{1 + \sin(\phi_m)} = 0.2464 \quad (13)$$

$$w_c^2 = zp \quad (14)$$

Now these equations can be solved to get

$$p = \sqrt{\frac{w_c^2}{z}} = 20.145, z = p \frac{z}{p} = 4.966 \quad (15)$$

Then k_c is chosen to ensure that the crossover frequency is at the desired value. This is done as follows:

$$K_c = \frac{1}{|G(jw_c) * G_d(jw_c)|} = 5.114 \quad (16)$$

Finally this gives a lead compensator

$$G_d = 5.114 \frac{\frac{s}{20.145} + 1}{\frac{s}{4.966} + 1} \quad (17)$$

The Bode plot of the compensated system is shown in Figure 5. It can be seen that the compensated system meets specifications.

Lag Compensator

A lag compensator is also designed, with the same specification of phase margin of ≥ 131 degrees and a steady state error of 1%. We shall call $D(s) = \frac{s+z}{s+p}$. Figure 4 can be used to find the frequency at $-180 + PM$, where PM is the desired phase margin, 131 degrees. Lag compensation will decrease the steady state error of the system, but unlike a lead compensator it does not improve the speed of the transient response. The frequency at this phase is about 0.692 radians/sec, and the magnitude at

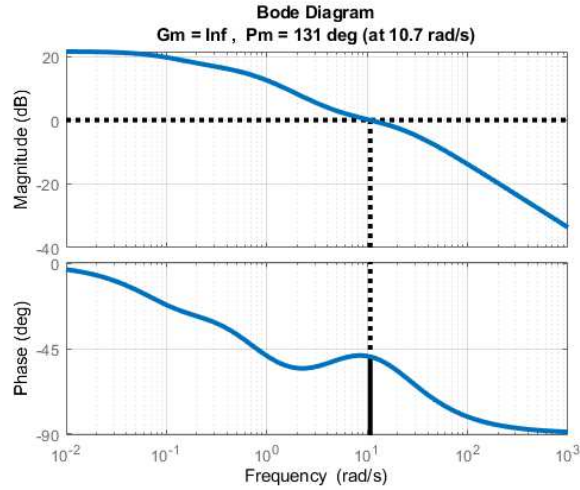


Figure 5. The Bode plot of the lead compensator on the linearized system. The resulting open loop transfer function is G_dG . Clearly the system meets the phase margin and crossover frequency specification.

this phase is $M = 1.0013$. This magnitude can be used to calculate K , since $K = \frac{1}{M} = \frac{1}{1.0013} = 0.9987$. Then a lag compensator is designed as follows:

$$e = \frac{1}{1 + KD(0)G(0)} = \frac{1}{1 + 2.33z/p} = \frac{1}{1 + 99} \quad (18)$$

where e is the desired steady state error. From there:

$$2.33 \frac{z}{p} = 99 \quad (19)$$

$$\frac{z}{p} = 42.4893 \quad (20)$$

We can choose a small z , such as $z = 0.001$, and then get $p = 2.3535e - 05$. Finally the lag compensator is

$$G_g(s) = KD_c(s) = 0.9987 \frac{s + 0.001}{s + 2.3535e - 05} \quad (21)$$

The Bode plot of the compensated system is shown in Figure 6. It can be seen that the compensated system meets the phase margin specification set. The error specification will be discussed later.

Lead-lag Compensator

Finally a lead-lag compensator is designed to get the benefits of both the lead and the lag compensation, meaning that it increases the speed of the transient response while also lowering the steady state error. The specifications are for the phase margin to be $PM \geq 131$ degrees, bandwidth frequency $w_{bw} \geq 10$ radians/second, and steady state error $e \leq 1\%$. The function $D_{lead}(s) = \frac{\frac{s}{z_{lead}} + 1}{\frac{s}{p_{lead}} + 1}$ is the lead part of the lead-lag compensator, which will be designed first. The same process used for the lead compensator can be used to obtain the lead zero and pole, $z_{lead} = 4.966$ and $p_{lead} = 20.145$. At the desired frequency w_{bw} , the magnitude of the Bode plot is $M \approx 0.1995$. This gives $K = M^{-1} = 5$. It can then be written as such:

$$KD_{lead}(s) = 5 \frac{\frac{s}{4.966} + 1}{\frac{s}{20.145} + 1} \quad (22)$$

Now the lag zero and pole are found using a similar process as the lag compensator.

$$e = \frac{1}{1 + KD_{lead}(0)G(0)} = \frac{1}{1 + 11.6652} \quad (23)$$

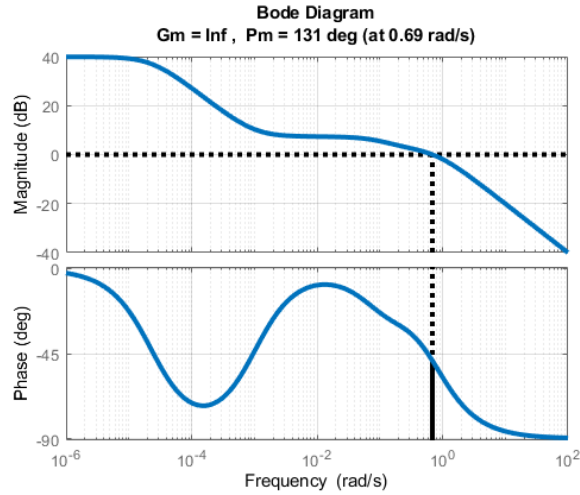


Figure 6. The Bode plot of the lag compensator on the linearized system. The resulting open loop transfer function is $G_g G$. Clearly the system meets the phase margin specification.

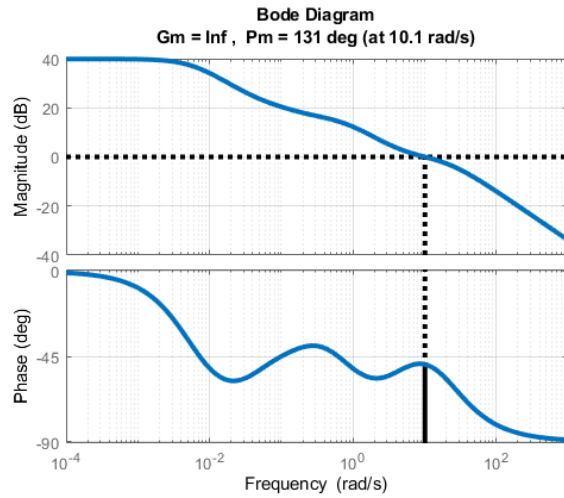


Figure 7. The Bode plot of the lead-lag compensator on the linearized system. The resulting open loop transfer function is $G_{leadlag} G$. Clearly the system meets the phase margin and crossover frequency specification.

where again e is the desired steady state error.

Comparing this to the desired error of $\frac{1}{1+99}$ shows that $D_{lead}(0) \geq \frac{99}{11.6652} = 8.4868$ with lag is desired. Thus $\frac{z_{lag}}{p_{lag}} = 8.4868$, or $p = \frac{z_{lag}}{8.4868}$. Then z_{lag} can be chosen to be 0.05, which is sufficiently small to not distort the phase lead. Then this gives $p_{lag} = 0.0059$.

$$G_{lead-lag}(s) = 5 \frac{\frac{s}{4.966} + 1}{\frac{s}{20.145} + 1} \frac{s + 0.05}{s + 0.0059} \quad (24)$$

From Figure 7, it is clear that the lead-lag compensated system meets the requirements for phase margin. The error specification will be discussed later.

Stability of the Linear Compensators on Nonlinear Model

For stability issues, it has been stated that for the time variant parameters in the model using linearization, all the local system are stable does not mean global stability⁴¹. This means that though the proposed compensators on the linearized model on the selected operating points are stable, the stability is not guaranteed for the entire parameter space (e.g., the variant model parameters on the other operating points) of the original nonlinear model. One method proposed in⁴² is to explore the parameter

subspace of the local model and use the grid point searching to iterate the process such that the entire parameter space can be covered. The grid points are the operating points used for linearization in current work. The parameter changes are treated as disturbances or small signals when linearizing at different operating points. The small-signal closed-loop transfer function can be obtained:

$$G_{cl}(z) = \frac{G(z)H(z)}{1 + G(z)H(z)}, \quad (25)$$

where $H(z)$ is the controller in z-domain, being transformed from continuous-time to discrete-time using bilinear transform $s = \frac{2(z-1)}{T(z+1)}$, where T is the numerical integration step size or sampling frequency. Based on the open loop transfer function $G(s)$ of the linearized model in Equation (10), the highest order of the plant is 4. For $H(z)$ being the lead or lag controller, the highest order in the denominator (i.e., the characteristic equation) of the closed loop local system is 5. And the denominator can be written in Equation (26).

$$\text{den}(G_{cl}(z)) = A \cdot z^5 + B \cdot z^4 + C \cdot z^3 + D \cdot z^2 + E \cdot z + F, \quad (26)$$

where A, B, C, D, E and F are functions of variable parameters $[V_0, n_0, m_0, h_0]$ (i.e., it is a 4 dimensional parameter space), and the designed values for compensator $[k, z, p, T]$. (Similarly, the lead-lag controller helps form the 6th order closed loop system.) For stability in z-domain, all the poles of the closed loop transfer function should be within the unit circle (i.e., radius $r < 1$). The open loop $G(s)$ is characterized by a local plant model parameter vector a_0 that is the vector of coefficients in $G(s)$ at the linearized points. So, the model parameter with perturbation q is $a = a_0 + q$. Stability requires the closed-loop poles to be inside the circle of radius r ($r < 1$), and three cases are considered:

$$z = r, \quad z = -r, \quad z = r(\cos\theta + j\sin\theta), \text{ where } \theta \in (-\pi, 0) \cup (0, \pi), \quad (27)$$

such that $\text{den}[G_{cl}(z, a)] = 0$. By substituting z values into Equation (26), equations consist of parameters $[V_0, n_0, m_0, h_0]$ delineate a circle bounded by radius r . The model parameters $[V_0, n_0, m_0, h_0]$ are treated as variables, and the design coefficients of the compensators remain constants during this process. This grid point method is iterated to search the different parameter subspaces (i.e., the linearized systems at different operating points used for designing the switching linear controllers) and ensures the combination of these subspaces cover the global parameter space. The global stability of the overall system is then obtained by iterating the grid-point searching until the local control laws cover all the local subsystems (i.e., the linearized system on specific operating points), and these local subsystems cover all the parameter spaces of the nonlinear system. Then the design coefficients of compensators are obtained to make sure the global stability of the closed loop system.

Besides, one can also obtain the stability of the nonlinear system by directly analyzing the symbolic transfer function of the linearized system, using the Jacobian matrix J_A (in Equation (6)) and J_B ($J_B = B$ in this particular case). All the parameters from the nonlinear model remain variables, and transfer function is derived, using formula $TF = C(sI - A)^{-1}B + D$. Similar to the procedures above, the plant transfer function has an order of 4, and with the lead compensator (order of 1), the closed loop transfer function has an order of 5. All the poles in the denominator of the closed loop transfer function should be negative (for a continuous time model). 5 solutions are obtained when solving for frequency variable s . Because the model parameters have numerical ranges based on their physical meanings, (i.e., n, m, h are the probabilities of channel opening/closing so that they are bounded within $[0, 1]$), these parameters are eliminated to obtain the worst case for the solutions of s , (i.e., at least one s is placed not in the left half plane in s-domain.) The design coefficients (i.e., i.e., the zero, pole and gain z, p, k of the compensator) are then chosen to make all of the solutions of s negative, which means the overall nonlinear plant is guaranteed stable with the controller.

Direct Nonlinear Control

Another controller will now be designed based on dynamic inversion, a method of direct nonlinear control, which does not require linearization of the system. The nonlinear system can be defined as

$$\dot{\vec{x}}(t) = f(\vec{x}) + g(\vec{x})u \quad (28)$$

and

$$y(t) = C\vec{x}(t) = h\vec{x} \quad (29)$$

where u is the control input that must be found. From Equation (1) and (2), we can define the values as follows

$$f(\vec{x}) = \begin{bmatrix} \frac{1}{C_m} \{G_K n^4 (E_K - V_m) + G_{Na} m^3 h (E_{Na} - V_m) + G_m (V_{leak} - V_m)\} \\ \alpha_n(V_m)(1-n) - \beta_n(V_m)n \\ \alpha_m(V_m)(1-m) - \beta_m(V_m)m \\ \alpha_h(V_m)(1-h) - \beta_h(V_m)h \end{bmatrix} \quad (30)$$

$$g(\vec{x}) = \begin{bmatrix} \frac{1}{C_m} \\ 0 \\ 0 \\ 0 \end{bmatrix} \quad (31)$$

and

$$C = [1 \quad 0 \quad 0 \quad 0] \quad (32)$$

The idea of dynamic inversion is to transform the coordinates such that the transformed system appears linear, and then a controller can be designed on this linear looking system.

Then u can be calculated as follows: The tracking error is defined as

$$Error = E(t) \triangleq y(t) - y^* \quad (33)$$

where y^* is the threshold voltage, denoted henceforth as V_{th} . Then select a fixed gain K such that

$$\dot{E} + KE = 0 \quad (34)$$

Here, the gain K is chosen to be 0.2, 0.5 and 1 to show the impact of different K values on the time responses. Using the definitions in Equation (28) to (33), \dot{E} can be found and plugged into Equation (34).

$$\dot{E} = \dot{y} = C\dot{\vec{x}} = C(f(\vec{x}) + g(\vec{x})u) \quad (35)$$

$$C(f(\vec{x}) + g(\vec{x})u) + K(C\vec{x} - V_{th}) = 0 \quad (36)$$

Equation (36) can now be solved for u .

$$u = (Cg(\vec{x}))^{-1} \{KV_{th} - Cf(\vec{x}) - KC\vec{x}\} \quad (37)$$

Plugging in the values for f , g , and C gives a final value of u as

$$u = KC_m V_{th} - G_K n^4 (E_K - V_m) - G_{Na} m^3 h (E_{Na} - V_m) - G_m (V_{leak} - V_m) - KV_m \quad (38)$$

A V_{th} of -55 mV will be used here. This controller can then be applied directly to the system, shown in Figure 15 and discussed in the next section.

Robust Incremental Dynamic Inversion

In this section, an incremental nonlinear dynamic inversion (IDNI)^{43,44} is applied to design the controller that is robust to model uncertainty. With the general system dynamics described in Equation (28) and (29), one can obtain the linearized HH model around a given pair of state and control inputs $[x_0, u_0]$, using the Taylor expansion that is truncated at the first-order term. Then the system dynamics at $[x, u]$ around this linearized point is as follows:

$$\begin{aligned} \dot{x} &\approx f(x_0) + g(x_0)u + \frac{\partial}{\partial x}[f(x) + g(x)u] |_{x=x_0, u=u_0} (x - x_0) + \frac{\partial}{\partial u}[f(x) + g(x)u] |_{x=x_0, u=u_0} (u - u_0) \\ &= \dot{x}_0 + J_A(x - x_0) + J_B(u - u_0) \end{aligned} \quad (39)$$

where J_A and J_B are the Jacobian matrix evaluated at the linearized point $[x_0, u_0]$. This approximation gives a linear dynamic in the neighborhood of the given operating point. Here we set the operating points equal to the sampling points, which means the non-linear system will be linearized at each sampling step. Different from the output dynamics in Equation (35), we now focus on the incremental terms $\Delta x = x - x_0$ and $\Delta u = u - u_0$, which are derived in Equation (40).

$$\dot{y} = C[\dot{x}_0 + J_A(x - x_0) + J_B(u - u_0)] \quad (40)$$

The incremental control law, which describes the control surface deflection changes, is then obtained as follows to make the output dynamics \dot{y} track the desired output dynamics \dot{y}_d :

$$\Delta u = u - u_0 = J_B^{-1}[y_d - C(x_0 + J_A(x - x_0))] \quad (41)$$

A sufficient control update rate can eliminate the error⁴⁴ $\Delta x = x - x_0$ in Equation (40). Then the full control law for the system is formed by accumulating the incremental control signals in Equation (42).

$$u = u_0 + \Delta u \quad (42)$$

Compared to the traditional nonlinear dynamic inversion controller in the reference¹⁸, this control law does not depend on the largest part of the HH model uncertainties, under the assumption that the control update rate is sufficient, such that the changes brought by $J_A(x - x_0)$ can be ignored. This increases the robustness of the system. In a mathematical representation, it means that for an uncertain model (Equation (43)), the uncertainties term $\Delta f(x)$ that is relevant to $x - x_0$ is negligible (given sufficient control update rate).

$$\dot{x} = f(x) + \Delta f(x) + g(x)u + \Delta g(x)u \quad (43)$$

For tracking purposes, the membrane potential is set to reach -55 mV from -70 mV in 1.5 ms. An exponential error decay dynamic is designed, which is $\gamma e^{t=1.5} = 70 - 55 = 15$. Then solving for γ results in $\gamma \approx 3.35$.

Model Predictive Control

The controllers designed above are not constrained by states and control input limits. In practice, the neuron may be damaged by current injections with large amplitudes, which implies that the input constraints should be considered when designing the controller. The model predictive control (MPC) is suitable to handle these constraints. The linear MPC algorithm can be applied to a linearized HH model that calculates the optimal control sequence, which drives the voltage V_m to the reference values.

A discrete time state space representation of the linearized model is obtained in Equation (44)

$$x(k+1) = Ax(k) + Bu(k), \quad x(0) = x_0, \quad (44)$$

where k is the current time step, and x_0 is the initial state. The running cost (or stage cost) at the i -th step is defined by

$$\ell(x_i, u_i) = \|x_i\|_Q^2 + \|u_i\|_{R_1}^2 + \|\Delta u_i\|_{R_2}^2 \quad (45)$$

where Q , R_1 and R_2 are the weighting matrix of states/output error, the control effort and the change in control move, respectively. Δu is the increment of control input. The cost function is defined by

$$J^\infty(x_0) = \sum_{i=0}^{\infty} \ell(x_i, u_i) = x_N^T P x_N + \sum_{i=0}^{N-1} (x_i^T Q x_i + u_i^T R_1 u_i + \Delta u_i^T R_2 \Delta u_i), \quad (46)$$

subject to $\underline{u} \leq u_i \leq \bar{u}, \quad \underline{x} \leq x_i \leq \bar{x}$,

where P is the terminal penalty matrix (i.e., the weight of the terminal state x_N), and $x_N^T P x_N$ corresponds to the infinite horizon cost. N is the prediction horizon that denotes the output of N steps in the future that will be predicted. The parameters $\underline{u}, \bar{u}, \underline{x}, \bar{x}$ are the lower and upper bounds of control input u and state x . The infinite prediction horizon is split into $[0, N-1]$ and $[N, \infty)$ shown in the second line in Equation (46). The quadratic programming is used to find the optimal control sequence $u_i, i = 0, 1, \dots, M-1$ (where M is the control horizon, and $M \leq N$) that minimizes the objective function J . A receding horizon policy is applied that only uses the first element in this control sequence as current control input, and then shifts the cost one time step forward to repeat this process. Note that in each step, only the first element u_0 in the control sequence is applied to the system. The synaptic noise is considered when designing the input constraints. For robust constraint satisfaction, we construct the robust input constraint set obtained using Minkowski difference $\mathbb{U}_{\mathbb{R}} = \mathbb{U} \ominus \mathbb{N}$, where $\mathbb{U}_{\mathbb{R}}, \mathbb{U}, \mathbb{N}$ are the robust

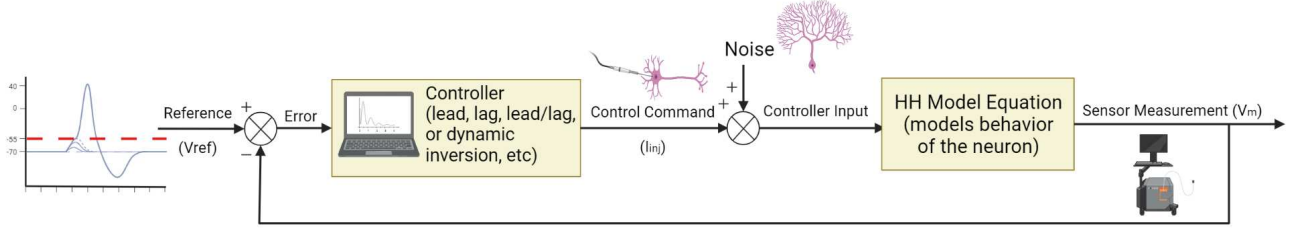


Figure 8. The block diagram of the controller on the nonlinear system (HH equations). Four controllers were used in this way: lead, lag, lead-lag, and dynamic inversion. Random synaptic noise is added when simulating the controller on the nonlinear system.

set of constraints, input constraints, synaptic noise set respectively and \ominus is the Minkowski set subtraction operator⁴⁵. We pick $Q = C^T C$ such that we focus on the state variable V_m . R_1 penalizes control efforts and R_2 penalizes control move changes, and they can be set as desired. Here we do not consider the control incremental part (i.e., $R_2 = 0$.)

The recursive feasibility must hold to ensure that a feasible control sequence (i.e., $\exists u$ that guarantees the prediction over the model satisfies all the constraints on states and inputs) exists when starting from a feasible initial point⁴⁶. Terminal constraint can be imposed to provide the recursive feasibility⁴⁵, such that the state at the end of the finite prediction horizon $N - 1$ should lie in a positively invariant set defined by model dynamics and the constraints. The infinite-horizon Linear Quadratic Regulator (LQR) can then be used to design the terminal constraints. The positive definite terminal weighting matrix P is computed as the solution of the discrete time Lyapunov Equation (47):

$$(A + BK)^T P(A + BK) = P - (Q + K^T RK), \quad (47)$$

where K is the terminal gain of the feedback control $u = Kx$ (i.e., the unconstrained LQR) that stabilizes the system starting from state x_N . The terminal region $T(x)$ is a set that all the state x within this set will be attracted to the origin asymptotically, where the local feedback control law policy takes over. The state before reaching this terminal set (i.e., $x_i \in \mathcal{X}, i = 0, \dots, N - 1$ from the initial states) needs to be steered to the terminal region by solving a constrained optimization sub-problem using quadratic programming. For example, an invariant terminal set can be an ellipsoidal set $T(x) = \{x \in R^n \mid x^T P x \leq 1\}$, or it can also be a polytopic set $T(x) = \{x \mid A_x x \leq b_x\}$. When dealing with model disturbance, a robust invariant set can be derived⁴⁷ to guarantee persistent feasibility and stability.

Then the stability is as follows. The objective function is decreasing, which guarantees the asymptotic stability and is shown below,

$$J_k^\infty = \sum_{i=0}^{\infty} \ell(x_i, u_i), \quad (48)$$

$$J_{k+1}^\infty = \sum_{i=1}^{\infty} \ell(x_i, u_i), \quad (49)$$

$$J_k^\infty - J_{k+1}^\infty = \ell(x_0, u_0) > 0. \quad (50)$$

The model is linearized at each sampling period such that the linear MPC can be applied. The terminal region and the terminal cost are computed each time to ensure stability and feasibility.

Results

Lead and Lag Compensator

All of the controllers designed were modeled in Matlab and Simulink in a closed loop feedback as described by Figure 8. This allows for the membrane voltage to be compared to a reference voltage, which is the input for the closed loop system.

When simulating the lead, lag, and lead-lag controllers on the non-linear system, the reference voltage of -55 mV is used for target tracking, and when the steady state is reached the controller is turned off, allowing the spike to occur. Random Gaussian white noise is also added to this input current for all simulations, as can be seen on the graphs, although on some plots it is harder to see than on others.

For the simulations of the lead, lag, and lead-lag controllers on the non-linear systems, the reference voltage will be a step function that creates a large error immediately, which would in turn result in a large spike in the current.

The tracking of the lead compensated system on the nonlinear system can be seen in Figure 9. As described before, once the reference voltage is increased and the membrane voltage reaches the threshold voltage, the controller is turned off allowing the voltage to spike.

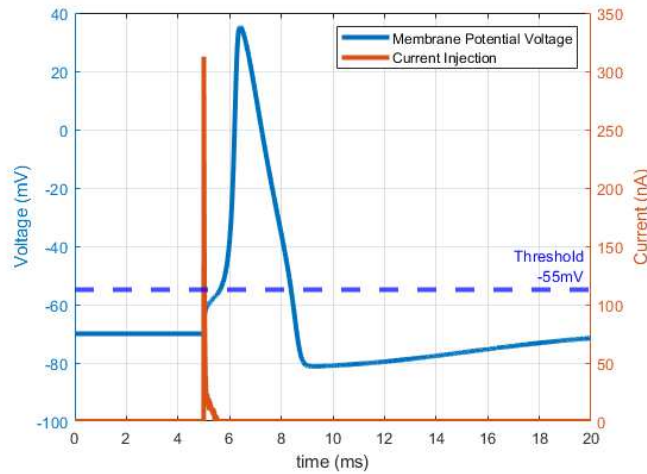


Figure 9. Lead compensator G_d used to track a reference voltage of -55 mV directly on the nonlinear system of Equations (1) and (2). The controller is initiated at $t = 5\text{ ms}$. Once this threshold voltage is reached the controller is turned off, allowing a spike to occur. The injected current produced by the controller with the addition of random Gaussian white synaptic noise is also plotted.

For the lag compensated system, the tracking of the reference voltage can be seen in Figure 10 on the nonlinear system. The lag compensated system takes longer to reach a steady state than the lead compensated system. Once again the voltage spikes once the controller is turned off.

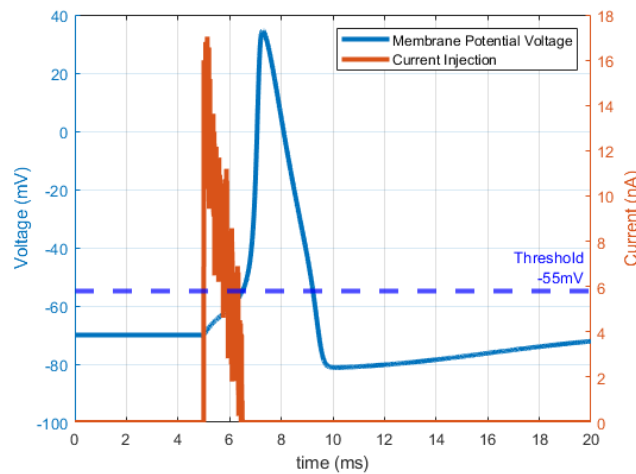


Figure 10. Lag compensator G_g used to track a reference voltage of -55 mV directly on the nonlinear system of Equations (1) and (2). The controller is initiated at $t = 5\text{ ms}$. Once this threshold voltage is reached the controller is turned off, allowing a spike to occur. The injected current produced by the controller with the addition of random Gaussian white synaptic noise is also plotted.

When the reference voltage is applied to the lead-lag compensated system, it can be seen through Equation (18) having the error be about 1.0%, which meets the specification. Also, the transient response is observed to be faster than that of lag. The tracking of this system can be seen in Figure 11 on the non-linear system. The non-linear system achieves no steady state error and spikes after the controller is turned off as described before. The robustness test of the lead, lag and the lead-lag controllers are shown in Figure 12, Figure 13 and Figure 14, respectively. The results show they are robust to 10% model

parameter uncertainties.

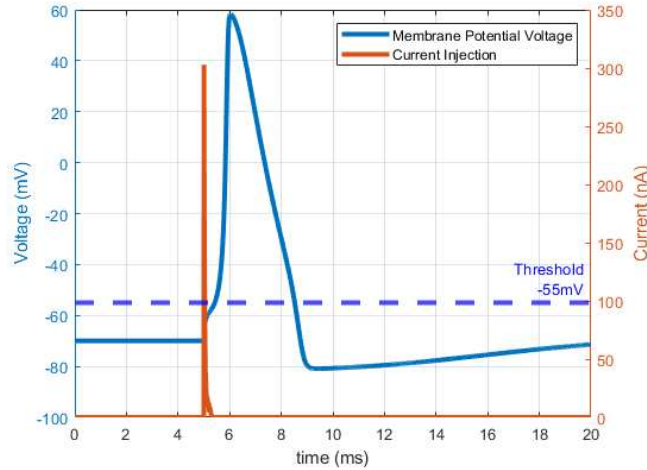


Figure 11. Lead-lag compensator $G_{lead-lag}$ used to track a reference voltage of -55 mV directly on the nonlinear system of Equations (1) and (2). The controller is initiated at $t = 5$ ms. Once this threshold voltage is reached the controller is turned off, allowing a spike to occur. The injected current produced by the controller with the addition of random Gaussian white synaptic noise is also plotted.

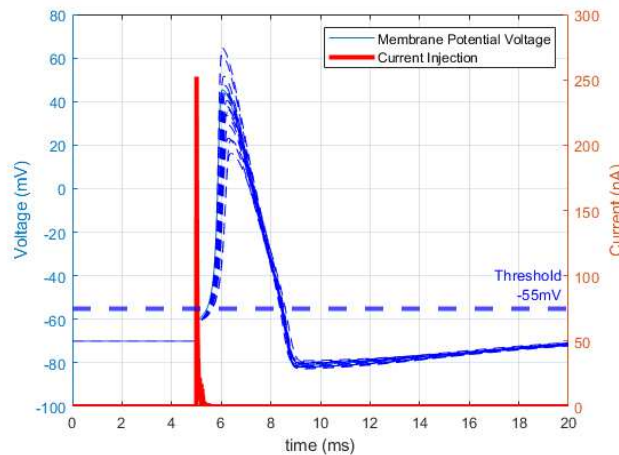


Figure 12. Robustness test for lead compensator. The uncertain model parameters are assumed to follow the normal distribution centered at the nominal parameter values, with 10% of nominal values as the variance. The control law based on the nominal model is applied to the models with these uncertain parameters for robustness test. The solid blue curve is the voltage output of the nominal model. The blue dotted curves show the output voltages from the uncertain models. Result shows the lead compensator is robust to the model uncertainties.

Dynamic Inversion

The dynamics of reference tracking using a dynamic inversion controller can be seen in Figure 15 (for the 1st order error dynamics). Smaller gain K results in less aggressive control behavior but the control action lasts for a longer time period. The voltage reaches a steady state at the reference voltage with perfect tracking.

Incremental Dynamic Inversion

Numerical simulation of the model and measurement uncertainty is carried out to validate the robustness of IDNI. Control laws are calculated based on the nominal HH model. The uncertain model parameters are assumed with 10% error, using

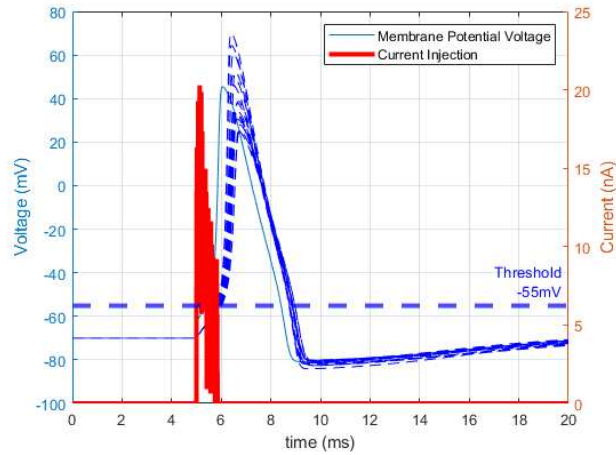


Figure 13. Robustness test for lag compensator. The uncertain model parameters are assumed to follow the normal distribution centered at the nominal parameter values, with 10% of nominal values as the variance. The control law based on the nominal model is applied to the models with these uncertain parameters for robustness test. The solid blue curve is the voltage output of the nominal model. The blue dotted curves show the output voltages from the uncertain models. Result shows the lag compensator is robust to the model uncertainties.

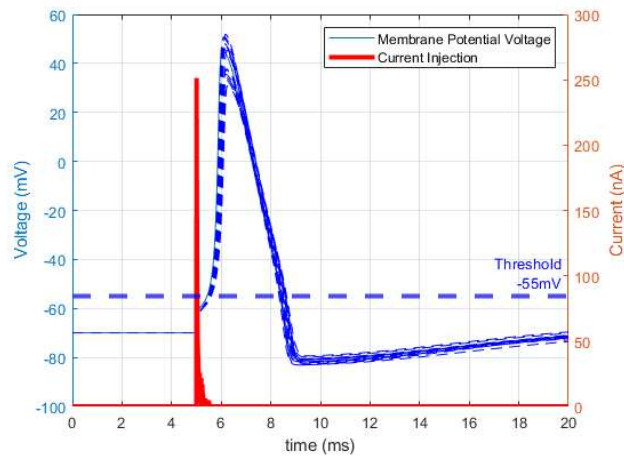


Figure 14. Robustness test for lead-lag compensator. The uncertain model parameters are assumed to follow the normal distribution centered at the nominal parameter values, with 10% of nominal values as the variance. The control law based on the nominal model is applied to the models with these uncertain parameters for robustness test. The solid blue curve is the voltage output of the nominal model. The blue dotted curves show the output voltages from the uncertain models. Result shows the lead-lag compensator is robust to the model uncertainties.

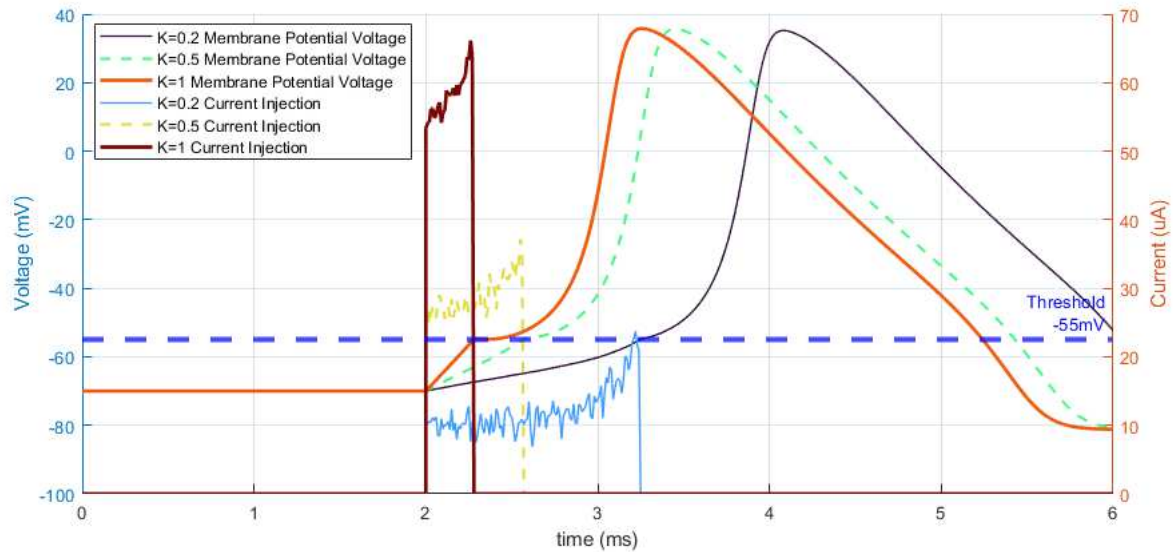


Figure 15. The dynamic inversion controller u used to track a reference voltage of -55 mV on the nonlinear system of Equations (1) and (2) ($K=0.2, 0.5$ and 1). The controllers are initiated at $t = 2$ ms. Then the controllers are turned off after a steady state is reached, allowing a spike to occur. The injected current produced by the controller with the addition of random Gaussian white synaptic noise is also plotted.

Gaussian distribution centered at its nominal values. The result is in Figure 16. It can be seen that the controller has robustness to HH model uncertainty, since the dynamic perturbation almost has no impact on reference tracking. It is found that the model uncertainty results in a slight time delay of neuron spiking. Also, the performance of tracking the reference is shown in Figure 17. Before reaching -55 mV, the voltage follows the predefined curve perfectly. After the threshold voltage is reached, the controller is turned off and the neuron spikes.

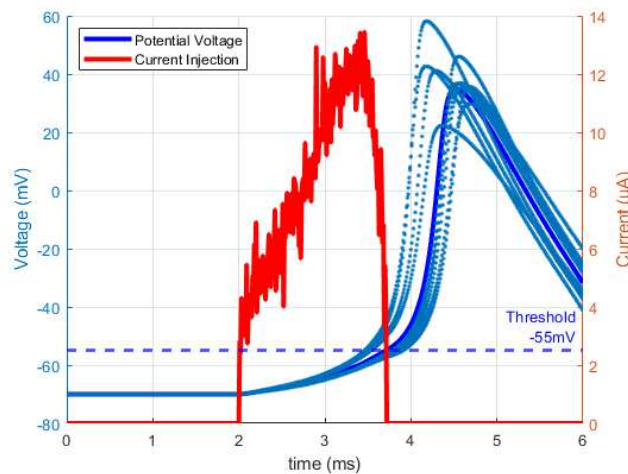


Figure 16. Incremental dynamic inversion is applied on the uncertain model. Note that the control command is calculated based on nominal model dynamics. The dynamics of applying the controllers to the uncertain model are in blue dotted curves. Due to uncertainty in model parameters, the dynamic behaviors (e.g., the maximal amplitude) of spiking vary.

Model Predictive Control

To simulate the HH dynamics with MPC control law in this section, linearization will be performed on the nonlinear system at each sampling point. Control input is constrained within $[0, 15]$ nA, and the membrane voltage V_m is contained within

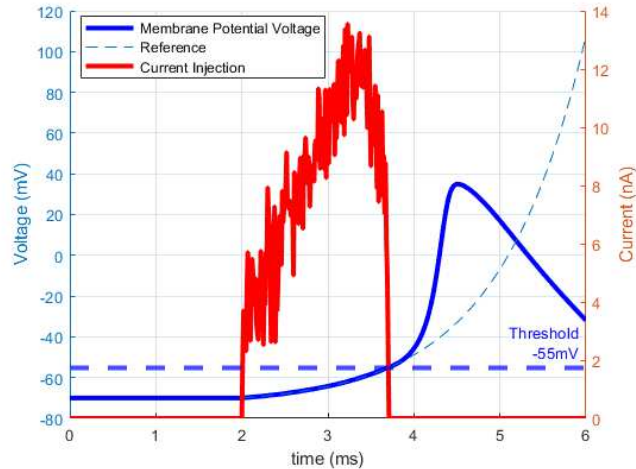


Figure 17. Reference tracking of IDNI controller. The membrane voltage tracks the predefined set points on the reference curve with the control law. After the voltage reaches -55 mV, the controller is turned off, allowing the neuron to spike based on HH model dynamics.

$[-70, -55]$ mV before the neuron spiking. Quadratic cost weighting matrices $Q = \text{diag}([5, 0.1, 0.1, 0.1])$ and $R_1 = 1$. Sampling time is picked as 0.01 ms, and both the control horizon M and prediction horizon N are set to 40 time steps (i.e., 0.4 ms) to ensure the recursive feasibility. The same reference (from Figure 17) is used here. It can be seen that the state error (i.e., the gap between the set points on reference and the model state) appears when placing the limit and penalties on the control effort. The robustness test is shown in Figure 18. The model uncertainties use the same settings.

Discussion

An activation spike in a neuron is when the voltage of the cell membrane reaches a threshold value, causing current to move from the axon of that neuron to the dendrite of another across the synapse. In this way information is moved from neuron to neuron. This spike can be controlled, meaning that the spike can be triggered at will, a method that has a variety of purposes including treatment for various neurological diseases, as well as helping to restore sight or hearing to those who are impaired.

Different model-based controllers were synthesized with the purpose of forcing a neuron to have this activation spike. Specifically the controllers are meant to determine the necessary current to be injected into the neuron cell membrane to reach the threshold voltage. Simulations of these controllers were done on a non-linear model of the neuron known as the Hodgkin-Huxley equations, as well as a linearized version of this system. These simulations were meant to show that the neuron could be forced to spike, and they did so.

All of the designed compensators were able to achieve low steady state error, according to the simulation, and the dynamic inversion controller achieved a settling time comparable to that of the lead and lead-lag controllers. Lead compensator is essentially a PD controller, and a lag compensator is essentially a PI controller. They provide specific gain and phase shift (i.e., change system's characteristic in the frequency domain). A PID controller handles the error/difference between the reference and the model output. However, linear controllers need a linear/linearized system. The performance is constrained around the operating points of linearization, since the controllers were designed on the linearized system, not the nonlinear system. However their error is still sufficiently low as to be acceptable. These controllers may not have robustness to model uncertainties or the actual nonlinear dynamics. They have good performance when simulating with nominal model parameters, but they may perform badly when the parameters are varying.

As for the nonlinear controllers, one obvious advantage is that it deals with nonlinearity of the system. The dynamic inversion control law is applied, different choices of error convergence for gain K are compared for dynamic inversion controller. The IDNI controller is then applied for robust control, since the largest part of model uncertainties are negligible when assuming the control update rate is sufficient. Compared to the existing state feedback controller from the reference¹⁸, whose design didn't take model uncertainties into consideration, the incremental dynamic inversion is robust to uncertain parameters in the model, which means the uncertainties will not change the controller behavior too much. The system output V_m is forced to follow a predefined rising curve. From the simulation, the uncertain parameter will only delay or advance the neuron spiking, due to the new model dynamics determined by these parameters. MPC is also applied to the HH model. MPC deals with a constrained optimization problem, using an objective function that consists of the weighted state and control input. The MPC

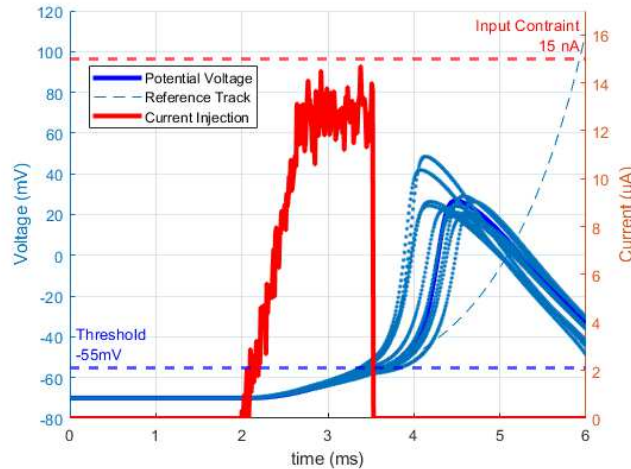


Figure 18. Robustness test on MPC with the performance of reference trajectory tracking. The upper limit of current injection \bar{u} is set as 15 nA. The state V_m is contained within $[-70, -55]$ mV. The control effort penalizes the reference tracking performance, which can be seen from the deviation of the system output V_m from the predefined exponential track (dotted curve). This deviation results in a delay of neuron spiking. The control sequence derived from the nominal model can still handle the reference tracking tasks and drive the neuron to spike.

applied in the current work is linearized at each sampling step, since the linear MPC algorithm only works for a linear model. Correspondingly, the terminal region and the terminal cost need to be updated each time for stability and feasibility. For sufficient sampling rate or frequency of doing linearization on the nonlinear model, the gap between the successive linear model can be eliminated.

The balance between state error and control efforts results in the deviation of system output V_m from the reference curve, and the neuron spiking is delayed consequently. The robustness and the ability of handling constraints would be significant in practical uses. In addition to neuron spiking controllers, some other control algorithms have been applied to the HH model for stabilizing the neuron, such as the bifurcation control⁴⁸.

The proposed lead and lag compensators haven't been used for neuron spiking before, though they are traditional. Our simulation validates the feasibility of applying such control strategies for neuron spiking. Besides the compensator design, to the best of our knowledge, we first applied incremental dynamics inversion to the HH model, and simulation shows it has a good reference tracking performance and robustness to model uncertainties. Model parameters are perturbed with 10% uncertainty for robustness test. Simulation shows the system with all the controllers designed above remains to be stable with allowable uncertainties.

From the simulation, the compensators result in current spikes with high amplitudes when given a fixed reference input. The tracking performances of the dynamic inversion and IDNI controllers to an exponentially rising curve show that they quickly reply to errors brought by reference inputs, and this causes the spikes after turning on the controllers. These controllers are more suitable when a fast tracking performance is desired. However, the control signals from MPC are driven not only by the reference trajectory, but also by the control efforts, according to its cost function. When turning on the controller, the control signals are increasing in a smooth way starting from 0 values. The MPC is thus superior to the dynamic inversion and IDNI in regards to this property. However, the computation complexity of MPC is more than that of the others. The choice of controller should depend on practical requirements.

Overall, the lead, lag, lead-lag, dynamic inversion, incremental dynamic inversion and model predictive control based control synthesis proved to be useful tools in generating controlled spiking of nonlinear neuronal dynamics in spite of underlying stochastic synaptic noise.

References

1. Csank, J. T., Soeder, J. F., Jeffrey C. Follo, M. J. M., Carbone, M. A. & Hau, Y. H. An autonomous power controller for the nasa human deep space gateway. *NASA Tech. Reports Serv.* (2018).
2. Antal, B., Mariano, B., Dun, M. & György, B. Closed-loop control of epilepsy by transcranial electrical stimulation. *Science* 735–737 (2012).

3. Gábor, K. & Antal, B. Sustained efficacy of closed loop electrical stimulation for long-term treatment of absence epilepsy in rats. *Sci. Reports* (2017).
4. Paz, J. T. *et al.* Closed-loop optogenetic control of thalamus as a tool for interrupting seizures after cortical injury. *Nat. Neurosci.* 64–70 (2013).
5. Krook-Magnuson, E., Armstrong, C., Oijala, M. & Soltesz, I. On-demand optogenetic control of spontaneous seizures in temporal lobe epilepsy. *Nat. Commun.* (2013).
6. Ehrens, D., Sritharan, D. & Sarma, S. V. Closed-loop control of a fragile network: application to seizure-like dynamics of an epilepsy model. *Front. neuroscience* (2015).
7. Durand, D. & Bikson, M. Suppression and control of epileptiform activity by electrical stimulation: A review. *Proc. IEEE* **89**, 1065 – 1082, DOI: [10.1109/5.939821](https://doi.org/10.1109/5.939821) (2001).
8. Choi, J. S. *et al.* Eliciting naturalistic cortical responses with a sensory prosthesis via optimized microstimulation. *J. Neural Eng.* (2016).
9. Fröhlich, F. & Jezernik, S. Annihilation of single cell neural oscillations by feedforward and feedback control. *J. computational neuroscience* **17**, 165–178 (2004).
10. Kiss, Z., Mooney, D., Renaud, L. & Hu, B. Neuronal response to local electrical stimulation in rat thalamus: physiological implications for mechanisms of deep brain stimulation. *Neuroscience* **113**, 137–143 (2002).
11. Santaniello, S., Fiengo, G., Glielmo, L. & Grill, W. M. Closed-loop control of deep brain stimulation: a simulation study. *IEEE Transactions on Neural Syst. Rehabil. Eng.* 15–24 (2011).
12. Frost, W. N. & Katz, P. S. Single neuron control over a complex motor program. *Proc. Natl. Acad. Sci.* **93**, 422–426 (1996).
13. Bidaye, S. S., Machacek, C., Wu, Y. & Dickson, B. J. Neuronal control of *Drosophila* walking direction. *Science* **344**, 97–101 (2014).
14. Barker, A. T. & Shields, K. Transcranial magnetic stimulation: basic principles and clinical applications in migraine. *Headache: The J. Head Face Pain* **57**, 517–524 (2017).
15. Eickenscheidt, M., Jenkner, M., Thewes, R., Fromherz, P. & Zeck, G. Electrical stimulation of retinal neurons in epiretinal and subretinal configuration using a multicapacitor array. *J. Neurophysiol.* (2012).
16. Grill, W. & Kirsch, R. Neuroprosthetic applications of electrical stimulation. *Assist. technology : official journal RESNA* **12**, 6–20, DOI: [10.1080/10400435.2000.10132006](https://doi.org/10.1080/10400435.2000.10132006) (2000).
17. Shepherd, R. K. & Javel, E. Electrical stimulation of the auditory nerve. i. correlation of physiological responses with cochlear status. *Hear. research* **108**, 112–144 (1997).
18. Fröhlich, F. & Jezernik, S. Feedback control of Hodgkin–Huxley nerve cell dynamics. *Control. engineering practice* **13**, 1195–1206 (2005).
19. Abbott, L. & Kepler, T. B. Model neurons: from Hodgkin-Huxley to Hopfield. In *Statistical mechanics of neural networks*, 5–18 (Springer, 1990).
20. FitzHugh, R. Impulses and physiological states in theoretical models of nerve membrane. *Biophys. journal* **1**, 445–466 (1961).
21. Rinzel, J. Excitation dynamics: insights from simplified membrane models. In *Fed. Proc.*, 15, 2944–2946 (1985).
22. Kepler, T. B., Abbott, L. & Marder, E. Reduction of conductance-based neuron models. *Biol. cybernetics* **66**, 381–387 (1992).
23. Joeken, S., Joeken, S., Joeken, S. & Schwegler, H. Predicting spike train responses of neuron models (1995).
24. Abbott, L. & van Vreeswijk, C. Asynchronous states in networks of pulse-coupled oscillators. *Phys. Rev. E* **48**, 1483 (1993).
25. Tsodyks, M., Mitkov, I. & Sompolinsky, H. Pattern of synchrony in inhomogeneous networks of oscillators with pulse interactions. *Phys. review letters* **71**, 1280 (1993).
26. Hopfield, J. J. & Herz, A. V. Rapid local synchronization of action potentials: Toward computation with coupled integrate-and-fire neurons. *Proc. Natl. Acad. Sci.* **92**, 6655–6662 (1995).
27. Ching, S. & Ritt, J. T. Control strategies for underactuated neural ensembles driven by optogenetic stimulation. *Front. Neural Circuits* (2013).

28. Ahmadian, Y., Packer, A. M., Yuste, R. & Paninski, L. Designing optimal stimuli to control neuronal spike timing. *J. Neurophysiol.* 1038–1053 (2011).
29. Liu, J., Khalil, H. K. & Oweiss, K. G. Model-based analysis and control of a network of basal ganglia spiking neurons in the normal and parkinsonian states. *J. Neural Eng.* (2011).
30. Dominquez, M. O., Gonía, J. & Netoff, T. I. Firing rate control of a neuron using a linear proportional-integral controller. *J. Neural Eng.* (2010).
31. Nandi, A., Kafashan, M. & Ching, S. Controlling point process generalized linear models of neural spiking. *Am. Control. Conf.* 5779–5784 (2016).
32. Iolov, A., Ditlevsen, S. & Longtin, A. Stochastic optimal control of single neuron spike trains. *J. Neural Eng.* (2014).
33. Grosenick, L., Marshel, J. H. & Deisseroth, K. Closed-loop and activity-guided optogenetic control. *Neuron* 106–139 (2015).
34. Paz, J. T. *et al.* Closed-loop optogenetic control of thalamus as a tool for interrupting seizures after cortical injury. *Nat. Neurosci.* 64–70 (2013).
35. Krook-Magnuson, E., Armstrong, C., Oijala, M. & Soltesz, I. On-demand optogenetic control of spontaneous seizures in temporal lobe epilepsy. *Nat. Commun.* (2013).
36. O'Connor, D. H. *et al.* Neural coding during active somatosensation revealed using illusory touch. *Nat. Neurosci.* 958–965 (2013).
37. Stark, E. *et al.* Pyramidal cell-interneuron interactions underlie hippocampal ripple oscillations. *Neuron* 467–480 (2014).
38. Sorokin, J. M. *et al.* Bidirectional control of generalized epilepsy networks via rapid real-time switching of firing mode. *Neuron* 194–210 (2017).
39. Wright, J., Macefield, V. G., van Schaik, A. & Tapson, J. C. A review of control strategies in closed-loop neuroprosthetic systems. *Front. neuroscience* **10**, 312 (2016).
40. Hodgkin, A. L. & Huxley, A. F. A quantitative description of membrane current and its application to conduction and excitation in nerve. *The journal physiology* **117**, 500–544 (1952).
41. Kvieska, P. N., Lebret, G. & Ait-Ahmed, M. Gain scheduled lqv systems-global vision and stability results. In *IAR/ACD08, workshop on Advanced Control and Diagnosis* (2008).
42. Amoozgar, M. H., Chamseddine, A. & Zhang, Y. Fault-tolerant fuzzy gain-scheduled pid for a quadrotor helicopter testbed in the presence of actuator faults. *IFAC Proc. Vol.* **45**, 282–287 (2012).
43. Sieberling, S., Chu, Q. & Mulder, J. Robust flight control using incremental nonlinear dynamic inversion and angular acceleration prediction. *J. guidance, control, dynamics* **33**, 1732–1742 (2010).
44. Chen, H. B. & Zhang, S. G. Robust dynamic inversion flight control law design. In *2008 2nd International Symposium on Systems and Control in Aerospace and Astronautics*, 1–6 (IEEE, 2008).
45. Dutta, A. *Design and certification of industrial predictive controllers* (Ghent University, 2014).
46. Kouvaritakis, B. & Cannon, M. Model predictive control. *Switzerland: Springer Int. Publ.* **38** (2016).
47. Dutta, A., Hartley, E., Maciejowski, J. & De Keyser, R. Certification of a class of industrial predictive controllers without terminal conditions. In *53rd IEEE Conference on Decision and Control*, 6695–6700 (IEEE, 2014).
48. Wang, J., Chen, L. & Fei, X. Bifurcation control of the hodgkin–huxley equations. *Chaos, Solitons & Fractals* **33**, 217–224 (2007).

Acknowledgments

The support from UConn School of Engineering and UTC - Institute for Advanced Systems Engineering is appreciated.

Author contributions statement

All authors contributed to the discussion of the contents, and reviewed and edited the manuscript

Declaration of Competing Interest

The authors declare that they have no competing interests.

Figures

Figure 1

A schematic of the neuron. Once the cell membrane reaches the threshold voltage, ions channels open allowing sodium and potassium ions to flow in and out, respectively. This results in the membrane voltage to spike, and an electric current moves across the synapse and is received by another neuron; this is how information is sent from neuron to neuron. The axon is the part of the neuron that carries the current away from the neuron, while the dendrite is what receives the current.

Figure 2

The circuit representation of the current flowing through a neuron membrane as described by the HH equations. The total current in the neuron is the sum of the current of each component of the circuit: the capacitor, the potassium, the sodium, a leakage current (G_m), and the injected current, I . The conductances G_K , G_{Na} , and G_m represent the ion channels and the voltage sources E_K , E_{Na} , and E_{leak} represent the equilibrium potentials.

Figure 3

Step responses of the linearized system. (For visualization purpose, the time response of voltages are transformed from relative displacement to absolute membrane voltages. And this transformation will be used in all the following plots of the time response simulation.) Four different operating points were chosen (between the resting voltage -70 mV and the threshold voltage -55 mV) to determine how the behavior of the system changed. From this four transfer functions were calculated, and their response to a step current ($I_{inj} = 8$ nA) is plotted here.

Figure 4

The Bode plot of the transfer function of the linearized system, G , is shown here. The Bode plot was used in designing lead, lag, and lead-lag controllers.

Figure 5

The Bode plot of the lead compensator on the linearized system. The resulting open loop transfer function is G_dG . Clearly the system meets the phase margin and crossover frequency specification.

Figure 6

The Bode plot of the lag compensator on the linearized system. The resulting open loop transfer function is G_lG . Clearly the system meets the phase margin specification.

Figure 7

The Bode plot of the lead-lag compensator on the linearized system. The resulting open loop transfer function is $G_{leadlag}G$. Clearly the system meets the phase margin and crossover frequency specification.

Figure 8

The block diagram of the controller on the nonlinear system (HH equations). Four controllers were used in this way: lead, lag, lead-lag, and dynamic inversion. Random synaptic noise is added when simulating the controller on the nonlinear system.

Figure 9

Lead compensator G_d used to track a reference voltage of -55 mV directly on the nonlinear system of Equations (1) and (2). The controller is initiated at $t = 5$ ms. Once this threshold voltage is reached the controller is turned off, allowing a spike to occur. The injected current produced by the controller with the addition of random Gaussian white synaptic noise is

also plotted.

Figure 10

Lag compensator G_l used to track a reference voltage of -55 mV directly on the nonlinear system of Equations (1) and (2). The controller is initiated at $t = 5$ ms. Once this threshold voltage is reached the controller is turned off, allowing a spike to occur. The injected current produced by the controller with the addition of random Gaussian white synaptic noise is also plotted.

Figure 11

Lead-lag compensator Glead-lag used to track a reference voltage of -55 mV directly on the nonlinear system of Equations (1) and (2). The controller is initiated at $t = 5\text{ ms}$. Once this threshold voltage is reached the controller is turned off, allowing a spike to occur. The injected current produced by the controller with the addition of random Gaussian white synaptic noise is also plotted.

Figure 12

Robustness test for lead compensator. The uncertain model parameters are assumed to follow the normal distribution centered at the nominal parameter values, with 10% of nominal values as the variance. The control law based on the nominal model is applied to the models with these uncertain parameters for robustness test. The solid blue curve is the voltage output of the nominal model. The blue dotted curves show the output voltages from the uncertain models. Result shows the lead compensator is robust to the model uncertainties.

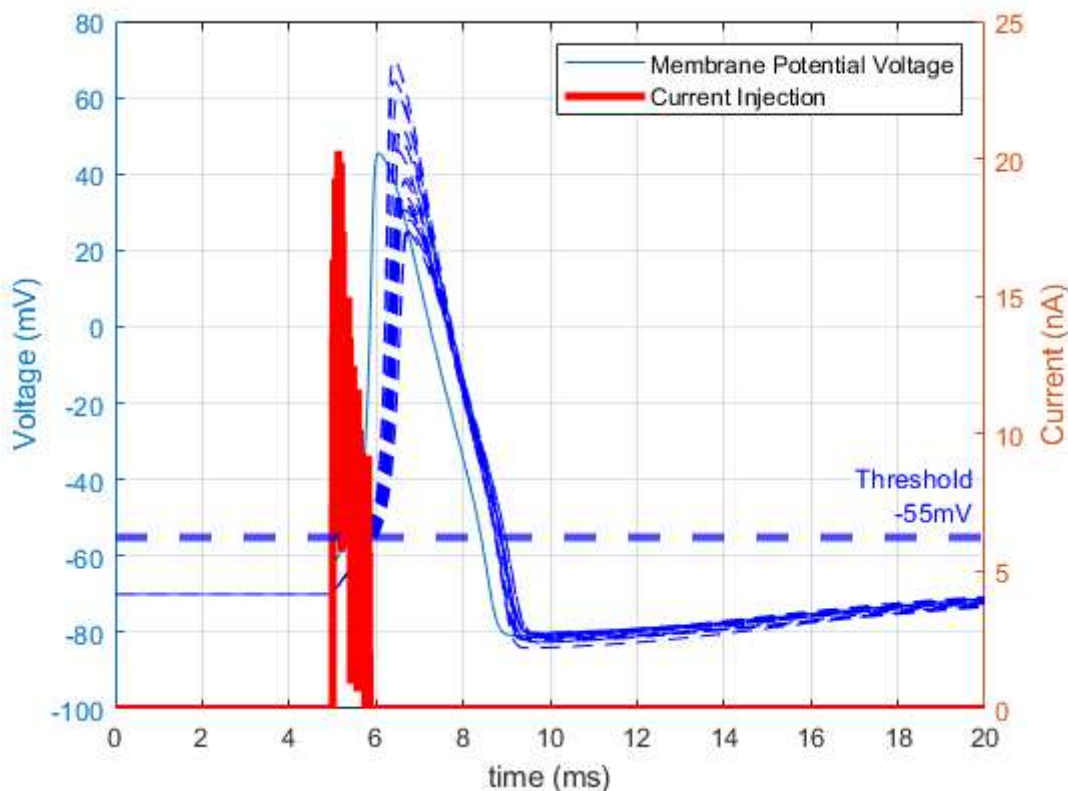


Figure 13

Robustness test for lag compensator. The uncertain model parameters are assumed to follow the normal distribution centered at the nominal parameter values, with 10% of nominal values as the variance. The control law based on the nominal model is applied to the models with these uncertain parameters for robustness test. The solid blue curve is the voltage output of the nominal model. The blue dotted curves show the output voltages from the uncertain models. Result shows the lag compensator is robust to the model uncertainties.

Figure 14

Robustness test for lead-lag compensator. The uncertain model parameters are assumed to follow the normal distribution centered at the nominal parameter values, with 10% of nominal values as the variance. The control law based on the nominal model is applied to the models with these uncertain parameters for robustness test. The solid blue curve is the voltage output of the nominal model. The blue dotted curves show the output voltages from the uncertain models. Result shows the lead-lag compensator is robust to the model uncertainties.

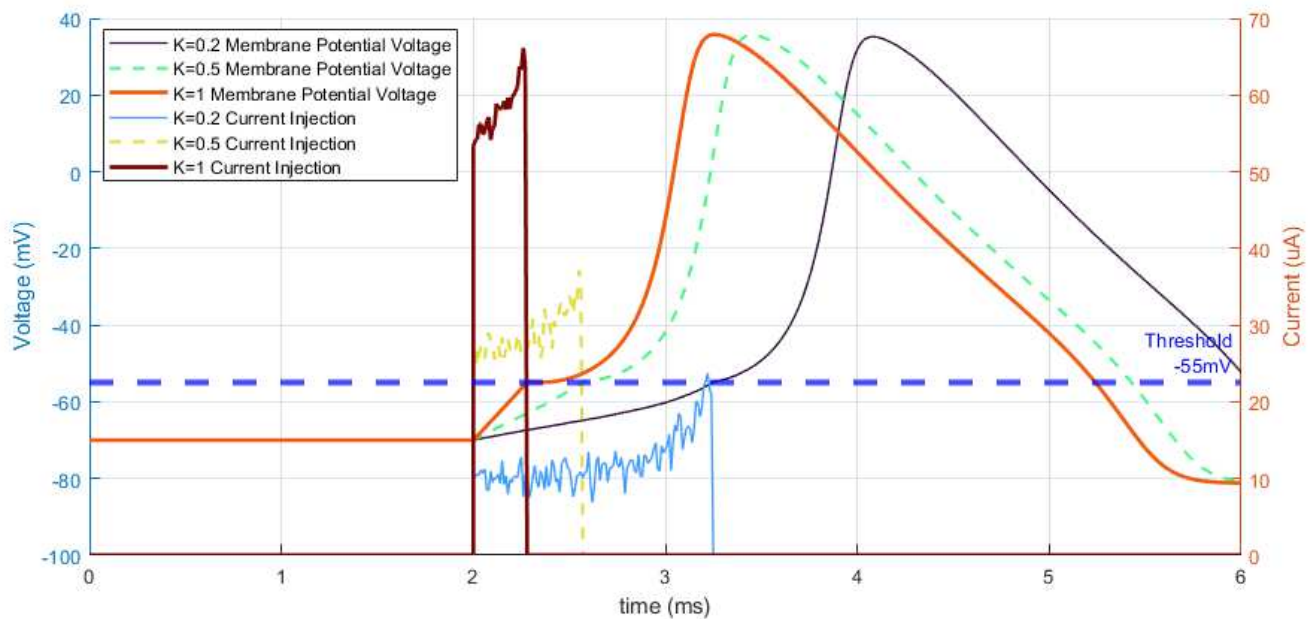


Figure 15

The dynamic inversion controller u used to track a reference voltage of -55 mV on the nonlinear system of Equations (1) and (2) ($K= 0.2, 0.5$ and 1). The controllers are initiated at $t = 2$ ms. Then the controllers are turned off after a steady state is reached, allowing a spike to occur. The injected current produced by the controller with the addition of random Gaussian white synaptic noise is also plotted.

Figure 16

Incremental dynamic inversion is applied on the uncertain model. Note that the control command is calculated based on nominal model dynamics. The dynamics of applying the controllers to the uncertain model are in blue dotted curves. Due to uncertainty in model parameters, the dynamic behaviors (e.g., the maximal amplitude) of spiking vary.

Figure 17

Reference tracking of IDNI controller. The membrane voltage tracks the predefined set points on the reference curve with the control law. After the voltage reaches -55 mV, the controller is turned off, allowing the neuron to spike based on HH model dynamics.

Figure 18

Robustness test on MPC with the performance of reference trajectory tracking. The upper limit of current injection u is set as 15 nA. The state V_m is contained within $[-70, -55]$ mV. The control effort penalizes the reference tracking performance, which can be seen from the deviation of the system output V_m from the predefined exponential track (dotted curve). This deviation results in a delay of neuron spiking. The control sequence derived from the nominal model can still handle the reference tracking tasks and drive the neuron to spike.